PHYSICAL REVIEW B **113**, 035131 (2026)

Local electronic structure and magnetic properties of double-perovskite $LaCo_{0.5}Ni_{0.5}O_3$ and $PrCo_{0.5}Ni_{0.5}O_3$

Meng-Jie Huang [1,2,*] Peter Nagel [1,3] Andreas Eich,[1] Michael Merz [1,3] and Stefan Schuppler[1,3]

[1] *Institute for Quantum Materials and Technologies, Karlsruhe Institute of Technology, Kaiserstraße 12, 76131 Karlsruhe, Germany*
[2] *Ruprecht-Haensel-Laboratory, Deutsches Elektronen-Synchrotron DESY, Notkestraße 85, 22607 Hamburg, Germany*
[3] *Karlsruhe Nano Micro Facility (KNMFi), Karlsruhe Institute of Technology, Kaiserstraße 12, 76131 Karlsruhe, Germany*

(Received 9 September 2024; revised 11 November 2025; accepted 5 January 2026; published 16 January 2026)

With x-ray absorption spectroscopy and x-ray magnetic circular dichroism, the element-specific electronic structure and the magnetic interactions of the double perovskite compounds $PrCo_{0.5}Ni_{0.5}O_3$ and $LaCo_{0.5}Ni_{0.5}O_3$ were studied. In both compounds, Co and Ni depart from their nominal valence state of +3, implying a charge transfer from Ni to Co. XMCD measurements clearly reveal a ferromagnetic behavior of Co and Ni in both samples. The substitution of La by Pr is isovalent but leads to a partial spin-state transition of Co^{3+} from high spin to low spin, resulting in a significant decrease in the magnetic moment of Co. Furthermore, a magnetic moment is found on the Pr site as well, with the Pr spin moment oriented antiparallel to those of Co and Ni. This antiferromagnetic coupling is induced by the superexchange interaction between the Pr $4f$ and Co/Ni $3d$ states.

DOI: 10.1103/7j4m-g6nh

I. INTRODUCTION

Transition-metal oxides with a perovskite-derived structure of the ABO_3 type [A, rare earth (RE); B, transition metal (TM)] display a wide range of physical properties including a host of insulating, superconducting, and magnetic phases. ABO_3 cobaltates, in particular, are well known to be prone to spin-state transitions [1–7], and among them $LaCoO_3$ (LCO) is the mother compound of a very versatile family of materials: not only does it exhibit temperature- and substitution-driven electronic and magnetic transformations [8–14] but is also useful as a cathode in high-temperature solid-oxide fuel cells [15–18]. The CoO_6 octahedra in LCO place the Co^{3+} ions in a local O_h symmetry, causing an e_g-t_{2g} splitting of the Co $3d$ orbitals by the crystal-field energy 10Dq. Because of the competition between 10Dq and Hund's exchange energy J_H the spin state of Co^{3+} can assume several configurations, including low-spin (LS; $t_{2g}^{\uparrow\downarrow\uparrow\downarrow\uparrow\downarrow}$, $S = 0$), high-spin (HS; $t_{2g}^{\uparrow\downarrow\uparrow\uparrow}e_g^{\uparrow\uparrow}$, $S = 2$), and intermediate-spin (IS; $t_{2g}^{\uparrow\downarrow\uparrow\downarrow\uparrow}e_g^{\uparrow}$, $S = 1$), with the nonmagnetic LS state generally favored at low temperature. This is why bulk LCO (among other undoped Co^{3+} cobaltates) shows no long-range magnetic ordering. Through "epitaxial-strain engineering", however, LCO and $PrCoO_3$ (PCO) can achieve ferromagnetic (FM) ordering: strain can effectively suppress the propensity of Co^{3+} to switch to LS at low temperature, leaving the HS fraction sufficiently large to support FM ordering [3,19–23]. Obviously, the Co^{3+} HS concentration plays a significant role in the magnetic behavior of cobaltates. A further avenue for tuning physical properties is partial substitution at the B site (Co site) by other TMs. FM ordering can also be established without resorting to epitaxial strain: in Ni-substituted LCO and PCO, for instance, such as in half-doped $LaCo_{0.5}Ni_{0.5}O_3$ (LCNO) and $PrCo_{0.5}Ni_{0.5}O_3$ (PCNO) [24–28]. Unlike La ions, which do not contribute to the magnetic interaction (owing to their completely unfilled $4f$ orbitals), Pr $4f$ electrons do participate to some degree in the magnetic interaction [22,28–32]. Investigation of the electronic structure of LCNO and PCNO enables us to understand the origin of the magnetic interactions in these compounds. Although several studies have probed the electronic structure of LCNO and PCNO, the reported results on their electronic structures are not fully consistent, and the detailed nature of the magnetic interactions in these systems remains a subject of discussion [24,26–28,33–38]. K-edge x-ray absorption spectroscopy has been applied to $LaCo_{1-x}Ni_xO_3$, but the interpretations also vary among reports. [26,35,38] The valence state was described either as +3 for both Co and Ni or as an increase of the Ni valence from Ni^{2+} to Ni^{3+} while the Co valence remains nearly constant with Ni doping. Viswanathan *et al.* further speculated on the electronic configuration based on temperature-dependent dc magnetization, suggesting possible Co^{3+} (IS)–Ni^{3+} (LS) or Co^{4+} (LS)–Ni^{2+} pairs [36]. Previous x-ray photoemission spectroscopy (XPS) studies on PCNO have revealed that cobalt exists in a mixed-valence state of Co^{3+} and Co^{4+}, while the Ni ions are predominantly close to a divalent state [27,28]. In contrast, another XPS study reported that both Co and Ni exhibit a mixture of 2+ and 3+ oxidation states, and that Pr contains a minor fraction of Pr^{4+} species [37]. These discrepancies highlight that the charge distribution and valence balance among Pr, Co, and Ni in PCNO, as well as the corresponding Co and Ni states in LCNO, remain controversial. This motivates a more

---

[*] Contact author: meng-jie.huang@desy.de

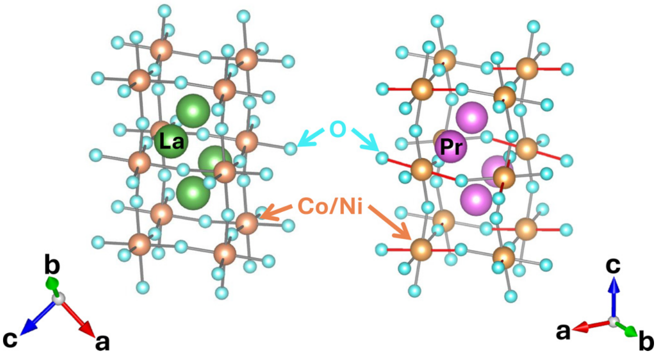

FIG. 1. Crystal structure of LCNO and PCNO visualized in the VESTA software [41,42] by using the lattice parameters *a*, *b*, and *c* derived from the XRD data. The LCNO crystal structure has been rotated to facilitate a more direct and intuitive comparison with PCNO.

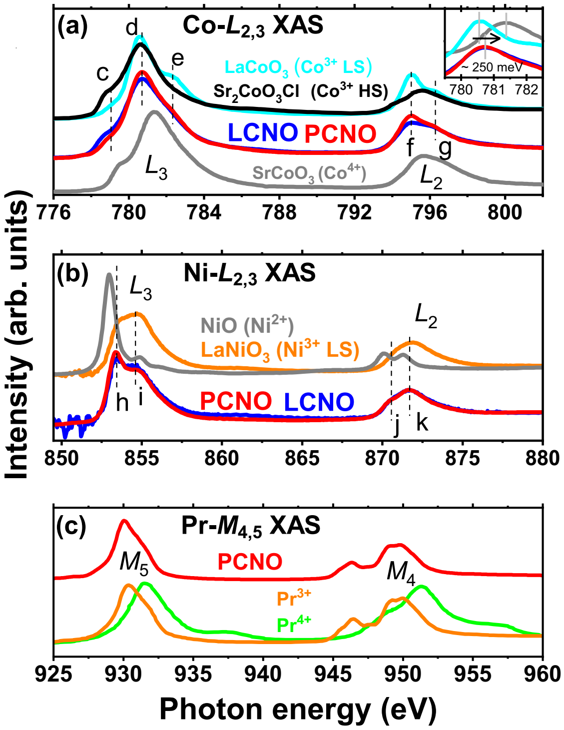

FIG. 2. (a) Co-$L_{2,3}$ XAS of LCNO and PCNO, together with reference spectra of LaCoO$_3$ (measured at 20 K, pure Co^{3+} LS), Sr$_2$CoO$_3$Cl (pure Co^{3+} HS, taken from Ref. [46]) and SrCoO$_3$ (Co^{4+}). The inset presents a comparison of the L$_3$ peak position between the studied samples and the reference spectra for Co^{3+} and Co^{4+}. (b) Ni-$L_{2,3}$ XAS of LCNO and PCNO, together with reference spectra of NiO (Ni^{2+}) and LaNiO$_3$ (Ni^{3+}). The La M_4 peak has been removed from the spectra, cf. Appendix B. (c) Pr-$M_{4,5}$ XAS together with the reference spectra of Pr^{3+} (Refs. [47–50]) and Pr^{4+} (Refs. [47,48]). Spectra are vertically shifted for clarity.

systematic investigation employing element-specific techniques with direct sensitivity to the 3*d* states, such as soft x-ray *L*-edge XAS and XMCD, to resolve the ambiguities left by previous *K*-edge XAS and XPS studies.

In this work, we therefore apply soft x-ray absorption spectroscopy (XAS) and x-ray magnetic circular dichroism (XMCD) on LCNO and PCNO to obtain direct and, above all, *element-specific* information on the valence structure, spin configuration, local symmetry, and FM interaction of the TMs, REs, and the light ligands in these compounds—effectively enabling us to identify and disentangle their interactions and magnetic properties.

II. SAMPLE AND EXPERIMENT

Polycrystalline samples of LaCo$_{0.5}$Ni$_{0.5}$O$_3$ and PrCo$_{0.5}$Ni$_{0.5}$O$_3$ were synthesized by stoichiometric mixtures of high purity powder of Co, Ni, La$_2$O$_3$, and Pr$_6$O$_{11}$ using the sol-gel method [39,40]. First, La$_2$O$_3$ and Pr$_6$O$_{11}$ powder were dried at 800 °C for 8 hours. The dried La$_2$O$_3$ and Pr$_6$O$_{11}$ were dissolved together with Co and Ni powder in a stoichiometric ratio in diluted nitric acid (32% HNO$_3$ of 70 ml). Diluted citric acid (30 ml deionized water + 5 g citric acid powder) was then added, and we concentrated this solutions by a slow evaporation at 100 °C while stirring. Next, the resulting solution was fired at 250 °C for 5 hours and at 500 °C for 10 hours in air to remove the carbonaceous species. After grinding in a mortar, the powders were further sintered in air at 950 °C for 30 hours and at 1050 °C for 48 hours. Finally, the powders were pressed into pellets. To ensure good oxygen stoichiometry the pellet samples were further sintered at 1050 °C in a flow of oxygen for 48 hours. X-ray diffraction (XRD) confirms the good sample quality. The detailed results of the XRD refinement analysis, including lattice parameters, bond lengths, bond angles, are provided in Appendix A. The crystal structure of LCNO and PCNO is visualized in Fig. 1 using the (relative) lattice parameters and distortions as determined by XRD.

Element-specific XAS and XMCD measurements at the O *K*, Co $L_{2,3}$, Ni $L_{2,3}$, and Pr $M_{4,5}$ edges were carried out at the Institute for Quantum Materials and Technologies (IQMT) beamline WERA at the KIT Light Source KARA (Karlsruhe, Germany). XAS was performed at temperatures of 300 K and 20 K, and XMCD was conducted at 20 K and with a magnetic field of ±4 T. All spectra were collected in the total-electron-yield detection mode. The degree of circular polarization of the incident light for XMCD was set to about 80%. The energy resolution was set to 0.15 eV, 0.35 eV, 0.4 eV, and 0.4 eV for the O *K*, Co $L_{2,3}$, Ni $L_{2,3}$, and Pr $M_{4,5}$ edge, respectively. Photon-energy calibration was ensured by adjusting the Ni-L_3 peak position determined on a NiO single crystal before and after each XAS or XMCD measurement [4,43]. For XMCD, absorption spectra were taken with the magnetic field oriented parallel (μ^+) and antiparallel (μ^-) to the x-ray beam; the XMCD spectrum is $\Delta\mu = \mu^+$-μ^-. Typically, spectra were also taken for both helicities, with identical results.

III. RESULTS AND DISCUSSION

Figures 2(a) and 2(b) exhibit the Co and Ni $L_{2,3}$ XAS spectra of LCNO and PCNO along with various reference spectra. Note that for LCNO, the huge La M_4 peak would almost completely overshadow the Ni L_3 signal and, to improve clarity, has been removed in this and the following figures.

(For details on this La-signal removal see Appendix B.) This is why the Ni-L_3 pre-edge background for LCNO appears less smooth than that of PCNO [44,45]. All XAS spectra are normalized in the post-edge range (Co, 805–810 eV; Ni, 885–890 eV; and Pr, 970–975 eV) where the absorption is atomic-like and featureless. The overall spectral features and shape of Ni XAS are very similar for LCNO and PCNO, and therefore no dramatic differences are to be expected in their local electronic structure with Ni character.For Co XAS, on the other hand, subtle but distinct spectral-weight changes are visible when comparing LCNO to PCNO. Three features (c, d, and e) are observed at the L_3 edge in Co XAS, and two more (f and g) at the L_2 edge. One can see that the intensity of peak c decreases, whereas peaks d and f increase when La is substituted by Pr. This spectral-weight change from LCNO to PCNO is similar to the differences seen between the reference systems Sr_2CoO_3Cl (SCOC, Co^{3+} HS) and LCO (Co^{3+} LS), implying a spin-state transition [4,46,51,52].

Accordingly, the differences observed for PCNO vs LCNO indicate a larger Co^{3+} LS fraction in the former. The XRD Rietveld refinement (see Table II) confirms that Pr substitution does not significantly affect the Co-O bond length. However, the Co-O-Co bond angle decreases by approximately by 5–6° compared to that of LCNO. This angular distortion is the underlying structural cause driving the stabilization of the Co^{3+} LS state in PCNO. A smaller Co-O-Co angle reduces the σ-type overlap between Co $3d$ and O $2p$ orbitals, thereby narrowing the e_g bandwidth and enhancing the 10Dq splitting relative to the J_H. As a result, the energy gain from adopting LS configuration becomes more favorable, leading to observed increase in the LS Co^{3+} population upon Pr substitution [53,54]. We exclude the Co^{3+} IS state in this study because the Co^{3+} IS configuration only exists in the case of strong tetragonal distortion [4,8,9]—and the XRD results on LCNO and PCNO do not provide any indication for such a strong distortion for either of them. The $L_{2,3}$ XAS of transition-metal oxides is also highly sensitive to changes in the valence state. A valence-state change from n to n + 1 leads to a significant energy shift of the L_3 peak to higher energies. This is illustrated in the inset of Fig. 2(a), superimposing the L_3 peak for Co^{3+} (LCO and SCOC) on that for Co^{4+} (SrCoO3): from Co^{3+} to Co^{4+} the L_3 peak moves to the high-energy side by about 1 eV. In the same inset, comparing now the L_3 peak position of PCNO and LCNO to that of LCO, an energy shift of about 0.25 eV to higher energy is clearly visible. This indicates that the Co valence in PCNO and LCNO is higher than 3+ ($Co^{+3+\epsilon}$); as a first rough estimate (and assuming an approximately linear scale) by about $\epsilon \sim +0.25$.

For Ni XAS, we observe a prominent peak i (k) on the high-energy side of L_3 (L_2), accompanied by a sharp peak h (shoulder peak j) located to the left of the main structure. It is obvious from the comparison of the spectra for LCNO and PCNO to those for the reference samples NiO (Ni^{2+}) and $LaNiO_3$ (Ni^{3+}) that peak i (peak k) corresponds to Ni^{3+}, whereas peak h (peak j) indicates Ni^{2+}. Taken together, it clearly suggests that the valence state of Ni is lower than 3+ ($Ni^{+3-\delta}$). The presence of both Co and Ni in a mixed-valence state shows a charge transfer from Ni to Co in LCNO and PCNO [25,27,28,55].

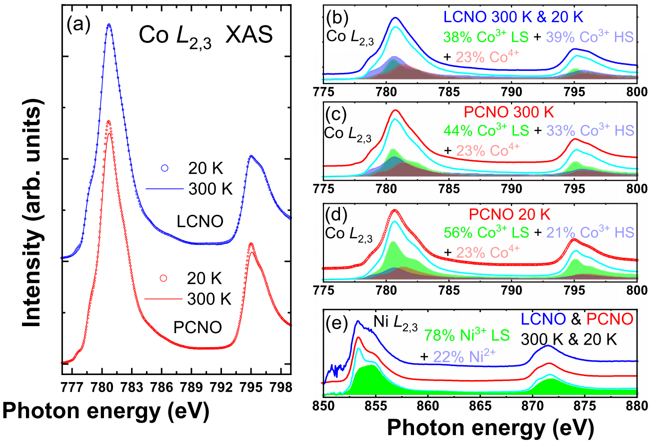

FIG. 3. (a) Temperature-dependent XAS of Co-$L_{2,3}$ for LCNO and PCNO. (b) XAS fitting for LCNO. We only show the fitting result for 300 K since the XAS data for 300 K and 20 K are identical. (c)(d) Fitting results for PCNO at 300 K and 20 K, respectively. (e) Fitting results at Ni-$L_{2,3}$ XAS. All blue and red solid lines represent the room-temperature spectra for LCNO and PCNO, respectively. Open symbols represent the XAS spectra taken at 20 K. Cyan lines are the fitting results.

The Pr-$M_{4,5}$ XAS as seen in Fig. 2(c) is identical to the reference spectrum of Pr^{3+} [48–50,56] and does not display any features commonly associated with Pr^{4+}[48,49]. This indicates that the La ion substitution by Pr in PCNO is isovalent. Together with the results from Ni ($Ni^{+3-\delta}$) and Co ($Co^{+3+\epsilon}$), the charge neutralization in both samples is nicely reflected also in the spectroscopic observations, further corroborating the valences observed. Considering the significant role of the Co^{3+} HS species for FM ordering in cobaltates, we also examine temperature-dependent XAS (T-XAS) to identify changes in the local electronic structure and, in particular, a possible evolution of the Co^{3+} HS fraction upon decreasing sample temperature. Figure 3(a) displays the Co-$L_{2,3}$ T-XAS measured at 300 K and 20 K. For LCNO, only minute changes are visible between 300 K and 20 K, suggesting that the valence and spin states of Co in LCNO remain essentially unchanged with temperature. For PCNO, on the other hand whose Co^{3+} HS fraction at 300 K is already lower to begin with, a further partial transition from HS to LS can be seen as the temperature decreases. Ni and Pr T-XAS of both samples do not exhibit any temperature-dependent changes [cf. Fig. 3(e) for Ni; not shown for Pr], and thus no changes of valence or spin state are expected on the Ni and Pr sites.

To better quantify the valence states and the Co^{3+} spin state we superimpose the reference XAS spectra in appropriate ratios to fit the Co and Ni XAS [4,8,57–63]. Figures 3(b)–3(d) displays the fitting result for Co. The Co valence state in both LCNO and PCNO and regardless of temperature is determined to be +3.23, with 77% of Co^{3+} and 23% of Co^{4+}. (Perhaps a little fortuitously, the rough estimate from the peak shift in Fig. 2 is quite similar.) For LCNO at both 300 and 20 K, the Co^{3+} HS concentration is found to be 39%. For PCNO, it decreases first to 33% at 300 K and then further and quite significantly to 21% at 20 K.

Figure 3(e) shows the XAS fitting for Ni; no spectral differences for the two compositions and the two temperatures can be identified. It should be noted that the peak h in L_3 of LCNO seems to have a slightly reduced intensity owing to the subtraction of the huge La M_4 background. As a result, the accuracy of fitting the Ni L_3 peak may be less reliable for LCNO. However, based on the spectral shape and energy position of the L_2, we can still conclude that the electronic structure of Ni of these two samples is nearly identical [64]. According to the fitting results of Ni XAS, we find that the valence state of Ni in both samples is about +2.78 (22% Ni^{2+} + 78% Ni^{3+}). This result indicates that both LCNO and PCNO exhibit a moderate charge disproportionation among the TMs, approximately following $\mathrm{Co}^{3+} + \mathrm{Ni}^{3+} \rightarrow \mathrm{Co}^{3.23+} + \mathrm{Ni}^{2.78+}$. Both Co and Ni thus remain close to trivalent states. Under these conditions, Co maintains a relatively localized $3d^6$-like electronic configuration, whereas Ni exhibits a more delocalized and strongly covalent character that can be described by a mixed $3d^8 + 3d^8\underline{L}$ configuration, where $\underline{L}$ denotes a ligand hole associated with oxygen $2p$ orbitals [65,66]. Such a redistribution of covalency between Co and Ni sites provides important insight into the microscopic origin of their distinct magnetic interactions in LCNO and PCNO. Meanwhile, the RE ions La^{3+} and Pr^{3+} also retain their nominal 3+ valence upon substitution, confirming that the primary charge redistribution occurs within the TM sublattice.

We turn now to the magnetic results we plot in Fig. 4, the μ^+ and μ^- XAS spectra and the resulting element-specific XMCD for LCNO and PCNO. (As mentioned before, the La M_4 peak interferes with Ni XMCD as well, and so special care was taken to minimize the residual noise in the Ni-L_3 region. For details see Appendix B.) In order to compare XMCD intensities across different elements more intuitively, all XMCD spectra were normalized to the absorption intensity at the energy position corresponding to the maximum XMCD signal at the L_3 (Co and Ni), M_5 (Pr), and K(O) edges. The resulting values are represented as percentages and plotted using a uniform y axis scale.

First, the Co XMCD spectra [Fig. 4(a)] for the two compounds exhibit comparable spectral shape, suggesting a common origin of the Co-based FM interaction in both. Also, the Co XMCD spectra show a negative sign at the L_3 peak, meaning that for both LCNO and PCNO, the Co spin moment aligns parallel to the external magnetic field. However, the Co XMCD amplitude decreases substantially from 2.6% for LCNO to 1.2% for PCNO. As mentioned above, FM ordering in cobaltates requires a sufficiently high Co^{3+} HS concentration, as illustrated by the following examples: (i) strain in epitaxial LCO (eLCO) thin films, "clamping" the low-temperature Co^{3+} HS fraction to ∼35%—which is a level sufficient to enable FM ordering [3]. (ii) LCO in powder and single-crystalline form with a Co^{3+} HS fraction $\leqslant 17\%$ at about 40 K, which is too low for FM order [3,8]. For PCNO, the XAS results of the preceding section show a Co^{3+} HS concentration of 21% at 20 K, only slightly higher than the value for example (ii). The drop in the Co XMCD intensities seen for PCNO can thus be mainly attributed to the low Co^{3+} HS concentration.

Ni XMCD exhibits the same dichroic sign to that of Co, and thus the Ni spin moment is ferromagnetically aligned to that of Co. Remarkably, the Ni L-edge XMCD is observed to be entirely unchanged, both in intensity and spectral shape, by the substitution of Pr for La—clearly indicating that the FM coupling at the Ni site remains the same (in contrast to the Co site). Pr-$M_{4,5}$ XMCD [Fig. 4(c)] also shows a significant dichroic signal. Its sign is opposite compared to Co and Ni, however, indicating that the Pr spin moment is antiparallel to the Co and Ni spin moment [22,23,67].

The ligand (oxygen) also plays an important role in mediating the magnetic interaction [68–74]. As $1s$ orbitals are not spin-orbit split, O-K XMCD will only determine the properties of the orbital moment. O-K XMCD spectra Fig. 4(d)] exhibit a negative peak at about 528.1 eV, showing that the orbital moment of the ligand oxygen is oriented parallel to that of Co and Ni. Further, one also observes that the O-K XMCD intensity significantly reduces from 2% for LCNO to 0.8% for PCNO. The $2p$ orbital of the ligand oxygen is polarized because of a transfer from polarized $3d$ orbitals of neighboring Co or Ni ions through p-d hybridization [21,68–74]. The reduced O-K XMCD intensity for PCNO

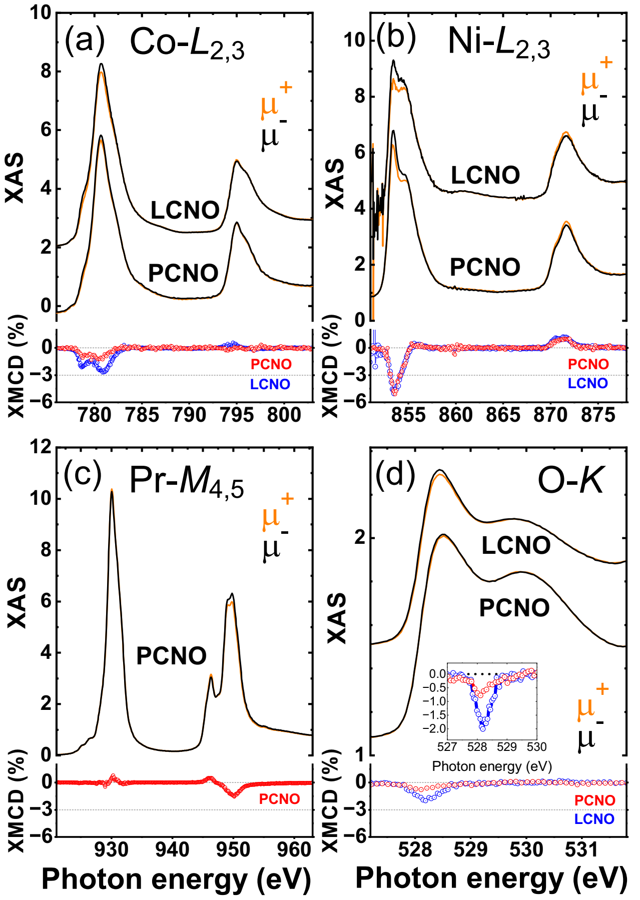

FIG. 4. The μ^+ and μ^- XAS together with the normalized XMCD (the normalization method for the XMCD spectra is described in main text) measured for the (a) Co-$L_{2,3}$, (b) Ni-$L_{2,3}$, (c) Pr-$M_{4,5}$, and (d) O-K edges. The inset of (d) displays the magnified version of the O-K XMCD spectra in the energy range 527–530 eV. All XMCD spectra are presented in a uniform y axis scale for the sake of comparison. In each panel, the XAS spectra for the different sample compositions are vertically offset for clarity.

can thus be directly attributed to the reduced Co magnetic moment.

By combining the results of XAS and XMCD, we may deduce the predominant exchange paths of the FM interactions. From the perspective of Ni, the FM interaction remains unaffected by both the Pr substitution and the concentration of Co^{3+} HS. This suggests that the ferromagnetic interaction occurring at the Ni site is established by the double-exchange (DE) interaction between Ni^{3+} and Ni^{2+}. For Co, the FM interaction is attributed to the DE interaction between Co^{3+} and Co^{4+}. In PCNO, there is an additional AFM interaction at work. According to Hund's rule, a free Pr^{3+} ($4f^2$) ion possesses two unpaired f electrons with a ground-state multiplet of $^3H_4$ and a ninefold degeneracy ($2J + 1 = 9$), corresponding to an effective magnetic moment of approximately 3.58 μ_B. In the orthorhombic *Pbnm* perovskite structure, the Pr^{3+} ion sits at the distorted 12-fold coordinated *A* site. The low-symmetry crystal field lifts the ninefold degeneracy ground state into nonmagnetic singlet [75–78]. Under these conditions, Pr^{3+} exhibits Van Vleck-type paramagnetism. Previous studies on Pr-based perovskites such as $PrCoO_3$ [79], $PrNiO_3$ [66,80–82], $PrMnO_3$, $PrCo_{1-x}Ni_xO_3$ [28], $Pr_{0.5}Sr_{0.5}MnO_3$ [83], Pr_2FeNiO_6 [84], and Pr_2NiMnO_6 [85–88] have reported that Pr^{3+} does not develop spontaneous magnetic order. Instead, in these perovskite compounds, the magnetic behavior (FM or AFM) is predominantly governed by the transition-metal sublattice (e.g., Ni-O-Mn, Ni-O-Ni, Ni-O-Fe, Co-O-Co, Mn-O-Mn), while Pr^{3+} only contributes a weak Curie-Weiss or Van Vleck-type paramagnetism. However, in PCNO, our XMCD measurements at 20 K reveal a finite Pr signal with a spin component that is antiparallel to the Co/Ni 3d moments, and with an intensity significantly larger than expected from a purely Van Vleck-type polarization (on the order of 10^{-3}-10^{-2} μ_B/atom). This indicates that the observed Pr magnetism cannot be attributed solely to field-induced paramagnetism, but instead requires an exchange field from the neighboring magnetically ordered Co and Ni sublattice to polarize the Pr^{3+} singlet ground state [22]. According to the Goodenough–Kanamori–Anderson rules, The antiparallel alignment between the Pr and the Co/Ni spin can be attributed to the ∼90° $4f$-$2p$-$3d$ superexchange (SE) pathways.

Applying the XMCD sum rules [89–97] to the XMCD spectra, we can further quantify the spin (m_s) and orbital (m_l) moments separately. (For details see Appendix C.) Table I lists the resulting values for m_s, m_l, total moment ($m_{tot} = m_s + m_l$), and the m_l/m_s ratio. We find that for Ni, none of these values (m_s, m_l, and m_l/m_s) show a discernible change upon replacing La by Pr as we have discussed in the XMCD section. For Co, on the other hand, m_s and m_l in PCNO are reduced to approximately 1/3 of the values for LCNO, which again can be attributed to the significant drop in the concentration of Co^{3+} HS. The ratio m_l/m_s for Co hardly changes, though (0.48 in LCNO, 0.54 in PCNO), and both m_l/m_s values are consistent with the possible range for Co^{3+}[8,25].

For Pr, we obtain m_s (–0.24 μ_B/atom) and m_l (0.30 μ_B/atom) values with opposite sign. Not unexpectedly, the localized nature of the Pr f orbitals leads to a relatively large orbital moment. Compared with Pr m_s, Pr m_l has a greater absolute value and is oriented parallel to the external magnetic field. The total moment m_{tot} remains aligned ferromagnetically with the external magnetic field. This finding is consistent with the result of bulk PCNO [28]. It is worth noting that although the free-ion Pr^{3+} is expected to exhibit $m_l/m_s = -3$; our XMCD analysis yields a much smaller value of approximately –1.2. This clear deviation from the atomic limit indicates that the Pr spin moment is not intrinsic but is induced by the internal exchange field from the magnetically ordered Co/Ni sublattice, rather than arising from a purely Van Vleck-type paramagnetic response.

TABLE I. Experimental spin moment (m_s), orbital moment (m_l), total moment ($m_{tot} = m_s + m_l$), and the orbital-to-spin ratio (m_l/m_s) in μ_B per atom derived from the XMCD sum-rule analysis. Here, we use $n_{3d} = 2.78$ and 4.25 for Ni and Co, respectively, and $n_{4f} = 12$ for Pr^{3+} in sum-rule analysis. Approximate error limits are shown in brackets (Ref. [98]).

		Magnetic moment (μ_B/atom)			
		m_s	m_l	m_{tot}	m_l/m_s
LCNO	Ni	0.31(2)	0.070(3)	0.38(1)	0.230(6)
	Co	0.23(1)	0.115(6)	0.34(2)	0.48(2)
PCNO	Ni	0.300(7)	0.070(2)	0.370(9)	0.230(6)
	Co	0.080(4)	0.043(2)	0.123(6)	0.54(3)
	Pr	−0.24(4)	0.30(5)	0.060(9)	−1.2(4)

IV. SUMMARY

With x-ray absorption spectroscopy (XAS) and x-ray magnetic circular dichroism (XMCD), the element-specific electronic and magnetic structure of the polycrystalline compounds $LaCo_{0.5}Ni_{0.5}O_3$ (LCNO) and $PrCo_{0.5}Ni_{0.5}O_3$ (PCNO) was studied to disentangle their magnetic interactions. Our spectroscopic results reveal the Co and Ni electronic structures, clarifying their valence and spin states. In both cases, Co and Ni exhibit charge disproportionation and a mixed-valence state according to $Co^{3+} + Ni^{3+} \rightarrow Co^{3.23+} + Ni^{2.78+}$. While substituting Pr for La has no discernible impact on the electronic structure of Ni, it does affect the Co^{3+} spin state: the latter is reduced from a (temperature-clamped) high-spin (HS) fraction of about 39% for LCNO to about 33% for PCNO at 300 K, which, depending now on temperature, drops to 21% at 20 K. This low HS fraction, in turn, explains the substantially reduced ferromagnetic interaction observed in Co L-edge XMCD for PCNO compared to LCNO. The XMCD reveals a ferromagnetic alignment of the spin moments of the Co and Ni sublattices. The magnetic properties of Pr are also complex. Its spin moment is oriented antiparallel to that of Co and Ni, consistent with a weak antiferromagnetic coupling mediated by the Co/Ni–O–Pr superexchange pathway, while its orbital moment aligns parallel to the transition-metal sublattice with a similar magnitude. Such an arrangement likely reflects the combined effects of a weak Van Vleck-type orbital polarization and an exchange-induced spin polarization driven by the neighboring Co/Ni-derived exchange field, resulting in an almost compensated but weakly ferromagnetic total Pr moment in PCNO.

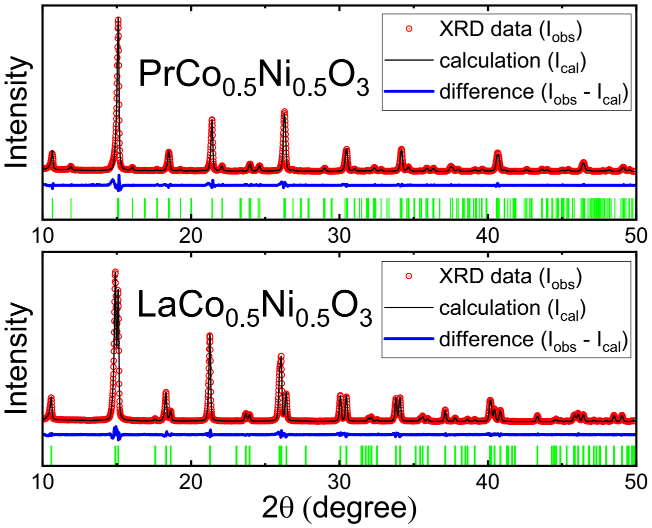

FIG. 5. Rietveld refined XRD pattern for $PrCo_{0.5}Ni_{0.5}O_3$ and $LaCo_{0.5}Ni_{0.5}O_3$, where the red hollow circles show the experimental data (I_{obs}), black lines represent the calculated spectra (I_{cal}), blue lines exhibit the difference (I_{obs}-I_{cal}), and green bars denote the position of the Bragg peaks. The difference patterns indicate good refinements for both samples.

ACKNOWLEDGMENTS

We gratefully acknowledge the KIT Institute for Beam Physics and Technology (IBPT) for operating the Karlsruhe Research Accelerator (KARA) storage ring and for providing beamtime at the KIT Light Source. We wish to thank Dr. Dirk Fuchs for introducing us to the sol-gel method and for performing the XRD measurements.

DATA AVAILABILITY

The data that support the findings of this article are not publicly available upon publication because it is not technically feasible and/or the cost of preparing, depositing, and hosting the data would be prohibitive within the terms of this research project. The data are available from the authors upon reasonable request.

APPENDIX A: X-RAY DIFFRACTION

XRD measurement was performed on the LCNO and PCNO samples in order to verify the sample quality. XRD was recorded at room temperature with Mo-K_{α_1} radiation and in the 2Θ range of 5° to 55° using a STOE STADI-P powder diffractometer. The XRD pattern shown in Fig. 5 indicates good sample quality for the PCNO and LCNO samples and proofs the absence of secondary phases. The observed diffraction peaks are consistent with a refinement in space group *Pbnm* for PCNO and $R\bar{3}c$ for LCNO, respectively. The lattice parameters *a* and *c*, the fractional atomic positions, the average bond distances ⟨*B*-O⟩, the average bond angles ⟨*B*-O-*B*⟩ (*B* is the central TM atom), the unit-cell volumes, and the reliability factors derived from the refinements are listed in Table II.

APPENDIX B: Ni XAS AND XMCD SPECTRA FOR $LaCo_{0.5}Ni_{0.5}O_3$

The large La-M_4 peak causes considerable difficulties in evaluating the Ni-$L_{2,3}$ XAS spectra. In the main text, only the "net" Ni-$L_{2,3}$ XAS spectra are therefore presented, where the La contribution has been subtracted from the "raw" Ni-$L_{2,3}$ XAS. The "pure" La-M_4 peak required for this is obtained from XAS taken in the Ni-$L_{2,3}$ range on LCO, as the crystal structure of LCO is very similar to that of LCNO. Figure 6 shows the La-M_4 peak for LCO and the raw Ni-$L_{2,3}$ XAS for LCNO. The resulting difference spectrum is plotted as the blue LCNO curve in Fig. 2(b).

For XMCD at the Ni *L*-edge, the problem is even more pronounced. Of course, La does not contribute to the XMCD signal, yet its high intensity can lead to strong background noise in the difference spectra, which may interfere with the precision of the Ni XMCD. Two different approaches were used for acquiring Ni XMCD spectra. The first is the standard XMCD scan strategy: apply a magnetic field parallel or antiparallel to the incident x-ray beam; scan the photon energy to measure the corresponding Ni-*L* edge XAS spectra (μ^+ and μ^-), cf. Fig. 7 (a); and take the difference (μ^+-μ^-) to obtain the Ni XMCD, which in this case is indicated by the blue line in the Fig. 7(b). The statistical noise in the La M_4 region (shaded in orange) is relatively small—but so is the Ni XMCD signal. In the second approach, the applied magnetic field was flipped between parallel and antiparallel orientation for each energy point in the XAS spectrum, so

TABLE II. Lattice parameters, volume, bond lengths and angles of LCNO and PCNO derived from the Rietveld refinement of the powder-diffraction data with the space group $R\bar{3}c$ and *Pbnm*, respectively.

Sample	*a* (Å)	*c* (Å)	Volume (Å^3)	Bond length ⟨*B*-O⟩ (Å)	Bond angle ⟨*B*-O-*B*⟩ (°)	R_{wp} (%)	R_p (%)	GOF (χ^2)
PCNO	5.4153(2)	7.6280(3)	223.69	1.942(4)	158.1(12)	8.0	4.9	2.78
				1.949(13)				
					158.0(8)			
				1.941(13)				
LCNO	5.46943(7)	13.1407(2)	393.1	1.9407(5)	163.86(18)	5.85	4.45	1.74

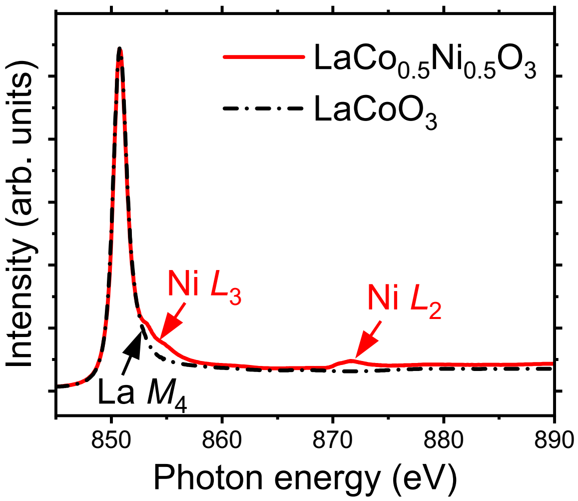

FIG. 6. The pure La-M_4 peak (dash dotted-black line) taken from Ni-free LCO and the raw Ni-$L_{2,3}$ XAS of LCNO (red line).

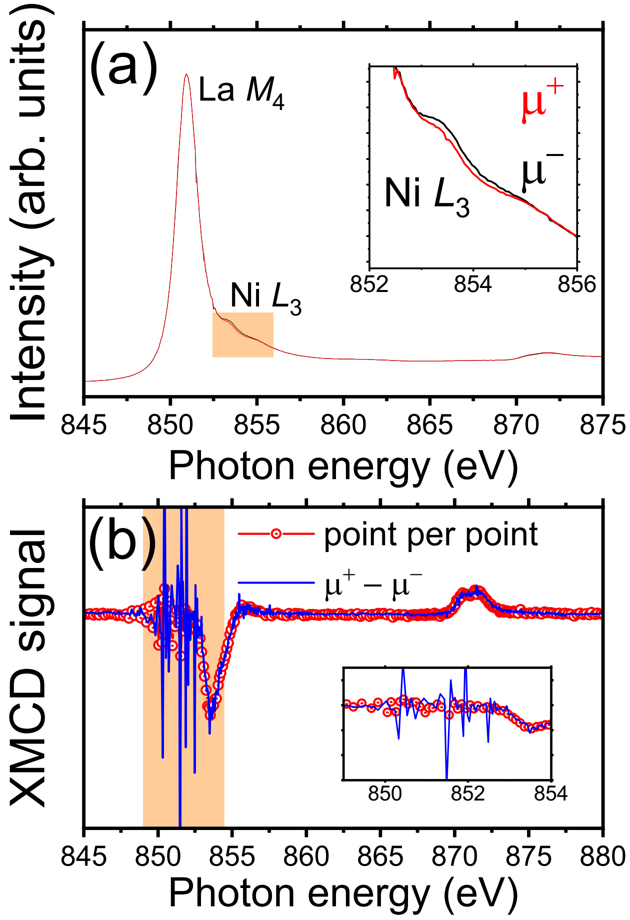

FIG. 7. (a) The raw Ni-$L_{2,3}$ XAS spectrum measured in magnetic filed either parallel (μ^+) and antiparallel (μ^-) to the x-ray beam. (b) The Ni L-edge XMCD resulting from the point-per-point scan strategy and from the conventional μ^+-μ^- method. The insets display the magnified version of the orange area.

that the μ^+ and μ^- spectra are obtained quasiconcurrently during the same photon-energy scan. The XMCD spectrum resulting from this "point-per-point" scan strategy is plotted in Fig. 7(b) as open red circles; this strategy turns out to be more effective than the standard one for minimizing the effect of the large La M_4 background on the Ni XMCD spectra.

APPENDIX C: XMCD SUM-RULE ANALYSIS

The XMCD sum-rule are, for the $L_{2,3}$ edges [89–95],

$$\begin{aligned} m_l &= -\frac{4\int_{L_3+L_2}(\mu^+-\mu^-)dE}{3\int_{L_3+L_2}(\mu^++\mu^-)dE}\times n_{3d} \\ &= -\frac{2}{3}\times\frac{(I_{L3}+I_{L2})}{A_L}\times n_{3d}, \\ m_s-7m_T &= -2\frac{\int_{L_3}(\mu^+-\mu^-)dE-2\int_{L_2}(\mu^+-\mu^-)dE}{\int_{L_3+L_2}(\mu^++\mu^-)dE} \\ &\quad\times n_{3d} \\ &= -\frac{I_{L3}-2I_{L2}}{A_L}\times n_{3d}, \end{aligned}$$

and for the $M_{4,5}$ edges [96,97],

$$\begin{aligned} m_l &= -2\frac{\int_{M_5+M_4}(\mu^+-\mu^-)dE}{\int_{M_5+M_4}(\mu^++\mu^-)dE}\times n_{4f} \\ &= -\frac{I_{M5}+I_{M4}}{A_M}\times n_{4f} \\ m_s-3m_T &= -\frac{\int_{M_5}(\mu^+-\mu^-)dE-\frac{3}{2}\int_{M_4}(\mu^+-\mu^-)dE}{\int_{M_5+M_4}(\mu^++\mu^-)dE} \\ &\quad\times n_{4f} \\ &= -\frac{I_{M5}-\frac{3}{2}I_{M4}}{2A_M}\times n_{4f}. \end{aligned}$$

Here, m_l and m_s represents the orbital and spin magnetic moment, respectively, in unit of μ_B/atom. The indices "L_3", "L_2", "M_5", and "M_4" of the integrals refer to the integration over the whole L_3, L_2, M_5, and M_4 edges. I_{L3}, I_{L2}, I_{M5} and I_{M4} represents the XMCD integration over the L_3, L_2, M_5, and M_4 region. A_L and A_M are the integrations of the whole polarization-averaged ("isotropic") XAS spectra (μ^+ + μ^-)/2. n_{3d} and n_{4f} represent the number of holes (i.e., the unoccupied states) in the Co(Ni) $3d$ and Pr $4f$ shells. In this study, we use $n_{3d} = 4.25$, $n_{3d} = 2.78$ and $n_{4f} = 12$ for Co, Ni and Pr, respectively, using the approximate fitting results discussed in the main text. m_T is the expectation value of the magnetic dipole operator for the ground state. In comparison to m_s, the m_T value for ion in octahedral symmetry is small and can be neglected [99]. Figure 8 displays the

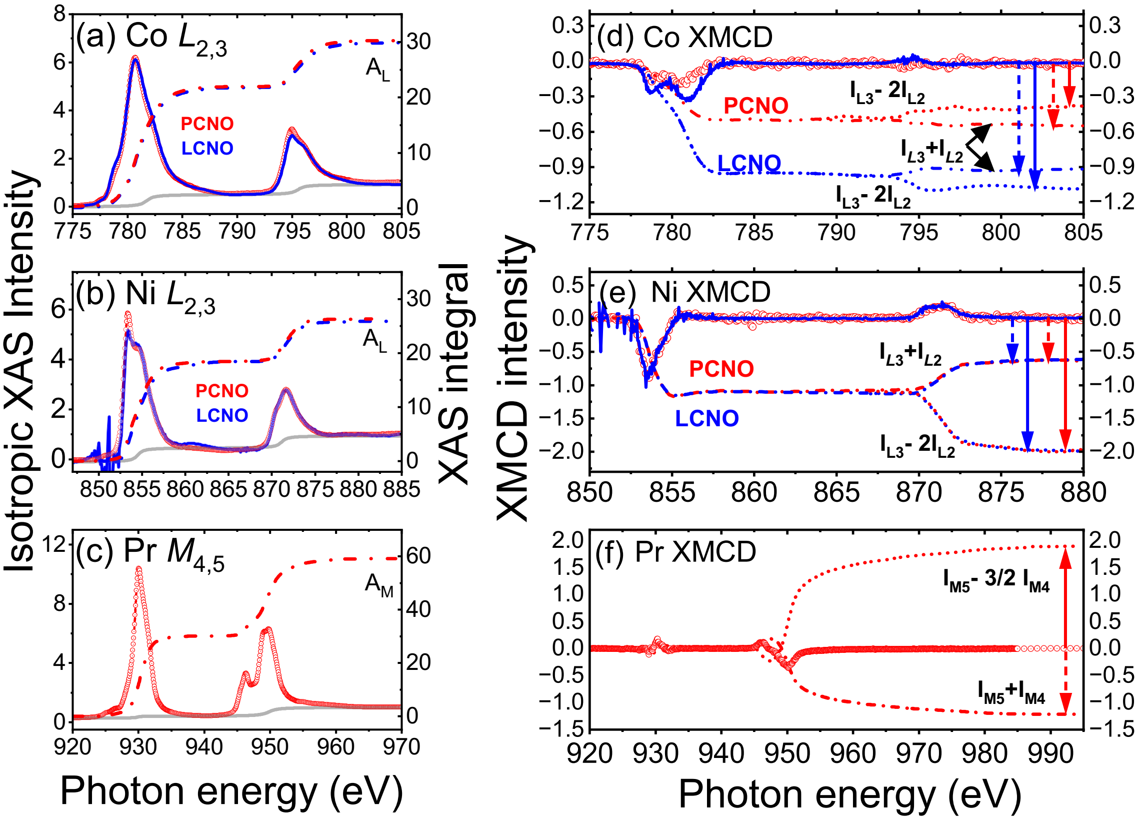

FIG. 8. (a)–(c) Isotropic XAS spectra ($\frac{1}{2}(\mu^+ + \mu^-)$) and the XAS integral ($\int(\mu^+ + \mu^-)dE$) of Co, Ni, and Pr for LCNO and PCNO. The grey line represents the background. (d)–(f) The resulting XMCD and the corresponding integration for the sum-rule analysis. The solid and dashed arrows represent the direction of the spin and orbital moments.

isotropic XAS, the integration of the isotropic XAS (A_L and A_M), the XMCD, and the corresponding integration values of the XMCD for the sum-rule analysis ($I_{L3} + I_{L2}$, $I_{L3} - 2I_{L2}$, $I_{M5} + I_{M4}$ and $I_{M5} - \frac{3}{2}I_{M4}$).

---

[1] M. Tachibana, T. Yoshida, H. Kawaji, T. Atake, and E. Takayama-Muromachi, Evolution of electronic states in RCoO$_3$ (R = rare earth): Heat capacity measurements, Phys. Rev. B **77**, 094402 (2008).

[2] Y. Ren, J.-Q. Yan, J.-S. Zhou, J. B. Goodenough, J. D. Jorgensen, S. Short, H. Kim, T. Proffen, S. Chang, and R. J. McQueeney, Spin-state transitions in PrCoO$_3$ studied with neutron powder diffraction, Phys. Rev. B **84**, 214409 (2011).

[3] C. Pinta, D. Fuchs, M. Merz, M. Wissinger, E. Arac, H. v. Löhneysen, A. Samartsev, P. Nagel, and S. Schuppler, Suppression of spin-state transition in epitaxially strained LaCoO$_3$, Phys. Rev. B **78**, 174402 (2008).

[4] M. Merz, P. Nagel, C. Pinta, A. Samartsev, H. v. Löhneysen, M. Wissinger, S. Uebe, A. Assmann, D. Fuchs, and S. Schuppler, X-ray absorption and magnetic circular dichroism of LaCoO$_3$, La$_{0.7}$Ce$_{0.3}$CoO$_3$, and La$_{0.7}$Sr$_{0.3}$CoO$_3$ films: Evidence for cobalt-valence-dependent magnetism, Phys. Rev. B **82**, 174416 (2010).

[5] I. A. Nekrasov, S. V. Streltsov, M. A. Korotin, and V. I. Anisimov, Influence of rare-earth ion radii on the low-spin to intermediate-spin state transition in lanthanide cobaltite perovskites: LaCoO$_3$ versus HoCoO$_3$, Phys. Rev. B **68**, 235113 (2003).

[6] S. K. Pandey, A. Kumar, S. Patil, V. R. R. Medicherla, R. S. Singh, K. Maiti, D. Prabhakaran, A. T. Boothroyd, and A. V. Pimpale, Investigation of the spin state of Co in LaCoO$_3$ at room temperature: *Ab initio* calculations and high-resolution photoemission spectroscopy of single crystals, Phys. Rev. B **77**, 045123 (2008).

[7] J. Herrero-Martín, J. L. García-Muñoz, K. Kvashnina, E. Gallo, G. Subías, J. A. Alonso, and A. J. Barón-González, Spin-state transition in Pr$_{0.5}$Ca$_{0.5}$CoO$_3$ analyzed by x-ray absorption and emission spectroscopies, Phys. Rev. B **86**, 125106 (2012).

[8] M. W. Haverkort, Z. Hu, J. C. Cezar, T. Burnus, H. Hartmann, M. Reuther, C. Zobel, T. Lorenz, A. Tanaka, N. B. Brookes, H.-H. Hsieh, H. J. Lin, C. T. Chen, and L. H. Tjeng, Spin state transition in LaCoO$_3$ studied using soft x-ray absorption spectroscopy and magnetic circular dichroism, Phys. Rev. Lett. **97**, 176405 (2006).

[9] A. Podlesnyak, S. Streule, J. Mesot, M. Medarde, E. Pomjakushina, K. Conder, A. Tanaka, M. W. Haverkort, and D. I. Khomskii, Spin-state transition in LaCoO$_3$: Direct neutron spectroscopic evidence of excited magnetic states, Phys. Rev. Lett. **97**, 247208 (2006).

[10] M. Itoh, M. Sugahara, I. Natori, and K. Motoya, Spin state and hyperfine interaction in LaCoO$_3$: NMR and magnetic susceptibility studies, J. Phys. Soc. Jpn. **64**, 3967 (1995).

[11] H. Hsu, P. Blaha, R. M. Wentzcovitch, and C. Leighton, Cobalt spin states and hyperfine interactions in LaCoO$_3$ investigated by LDA+U calculations, Phys. Rev. B **82**, 100406(R) (2010).

[12] M. A. Korotin, S. Y. Ezhov, I. V. Solovyev, V. I. Anisimov, D. I. Khomskii, and G. A. Sawatzky, Intermediate-spin state and properties of LaCoO$_3$, Phys. Rev. B **54**, 5309 (1996).

[13] R. F. Klie, J. C. Zheng, Y. Zhu, M. Varela, J. Wu, and C. Leighton, Direct measurement of the low-temperature spin-state transition in LaCoO$_3$, Phys. Rev. Lett. **99**, 047203 (2007).

[14] A. Laref and S. J. Luo, Magnetic excitation and phonon dispersion in LaCoO$_3$ compound, J. Phys. Soc. Jpn. **79**, 064702 (2010).

[15] D. Baskar and S. B. Adler, High temperature magnetic properties of Sr-doped lanthanum cobalt oxide (La$_{1-x}$Sr$_x$CoO$_{3-\delta}$), Chem. Mater. **20**, 2624 (2008).

[16] S. J. Skinner, Recent advances in Perovskite-type materials for solid oxide fuel cell cathodes, Int. J. Inorg. Mater. **3**, 113 (2001).

[17] J. M. Ralph, C. Rossignol, and R. Kumar, Cathode materials for reduced-temperature SOFCs, J. Electrochem. Soc. **150**, A1518 (2003).

[18] E. Maguire, B. Gharbage, F. M. B. Marques, and J. A. Labrincha, Cathode materials for intermediate temperature SOFCs, Solid State Ionics **127**, 329 (2000).

[19] A. Posadas, M. Berg, H. Seo, A. de Lozanne, A. A. Demkov, D. J. Smith, A. P. Kirk, D. Zhernokletov, and R. M. Wallace, Epitaxial integration of ferromagnetic correlated oxide LaCoO$_3$ with Si (100), Appl. Phys. Lett. **98**, 053104 (2011).

[20] H. Seo, A. Posadas, and A. A. Demkov, Strain-driven spin-state transition and superexchange interaction in LaCoO$_3$: *Ab initio* study, Phys. Rev. B **86**, 014430 (2012).

[21] D. Fuchs, E. Arac, C. Pinta, S. Schuppler, R. Schneider, and H. v. Löhneysen, Tuning the magnetic properties of LaCoO$_2$ thin films by epitaxial strain, Phys. Rev. B **77**, 014434 (2008).

[22] V. V. Mehta, S. Bose, J. M. Iwata-Harms, E. Arenholz, C. Leighton, and Y. Suzuki, Ferrimagnetism in PrCoO$_3$ epitaxial films, Phys. Rev. B **87**, 020405(R) (2013).

[23] T. D. Sanders, U. S. Alaan, M. T. Gray, S. Bose, M. Taylor, M. Cabero, V. Mehta, M. Varela, C. Leighton, and Y. Suzuki, Magnetism in epitaxial PrCoO$_3$ and Pr$_{0.7}$Y$_{0.3}$CoO$_3$ thin films, J. Magn. Magn. Mater. **451**, 654 (2018).

[24] T. Wu, G. Wu, and X. H. Chen, Effect of disorder on transport and electronic structure in LaCo$_{1-x}$Ni$_x$O$_3$ system, Solid State Commun. **145**, 293 (2008).

[25] P. K. Sreejith, T. S. Suraj, H. B. Vasili, S. Sreya, P. Gargiani, K. Sethupathi, O. Cespedes, V. Sankaranarayanan, and M. S. R. Rao, Spin reorientation induced anisotropic magnetoresistance switching in LaCo$_{0.5}$Ni$_{0.5}$O$_{3-\delta}$ thin films, Phys. Rev. B **107**, 224425 (2023).

[26] T. Kyômen, R. Yamazaki, and M. Itoh, Valence and spin state of Co and Ni ions and their relation to metallicity and ferromagnetism in LaCo$_{0.5}$Ni$_{0.5}$O$_3$, Phys. Rev. B **68**, 104416 (2003).

[27] A. Ahmed and B.-S. Choi, Influence of Ni substitution on the magnetic properties of PrCoO$_3$: A comprehensive study, Mater. Chem. Phys. **307**, 128232 (2023).

[28] P. Tomeš, M. H. Aguirre, R. Robert, A. Shkabko, E. H. Otal, and A. Weidenkaff, Transport and magnetic properties of PrCo$_{1-x}$Ni$_x$O$_3$ ($x = 0.0$-0.7), J. Phys. D **44**, 305402 (2011).

[29] C. Leighton, D. D. Stauffer, Q. Huang, Y. Ren, S. El-Khatib, M. A. Torija, J. Wu, J. W. Lynn, L. Wang, N. A. Frey, H. Srikanth, J. E. Davies, K. Liu, and J. F. Mitchell, Coupled structural/magnetocrystalline anisotropy transitions in the doped perovskite cobaltite Pr$_{1-x}$Sr$_x$CoO$_3$, Phys. Rev. B **79**, 214420 (2009).

[30] J. L. García-Muñoz, J. Padilla-Pantoja, X. Torrelles, J. Blasco, J. Herrero-Martín, B. Bozzo, and J. A. Rodríguez-Velamazán, Magnetostructural coupling, magnetic ordering, and cobalt spin reorientation in metallic Pr$_{0.5}$Sr$_{0.5}$CoO$_3$ cobaltite, Phys. Rev. B **94**, 014411 (2016).

[31] A. M. Balagurov, I. A. Bobrikov, V. Y. Pomjakushin, E. V. Pomjakushina, D. V. Sheptyakov, and I. O. Troyanchuk, Low-temperature structural anomalies in Pr$_{0.5}$Sr$_{0.5}$CoO$_3$, JETP Lett. **93**, 263 (2011).

[32] J. Padilla-Pantoja, J. L. García-Muñoz, B. Bozzo, Z. Jirák, and J. Herrero-Martín, Structural properties and singular phase transitions of metallic Pr$_{0.5}$Sr$_{0.5}$CoO$_3$ cobaltite, Inorg. Chem. **53**, 12297 (2014).

[33] H. Kozuka, K. Ohbayashi, and K. Koumoto, LaCo$_{1-x}$Ni$_x$O$_3$ with improved electrical conductivity, Inorg. Chem. **51**, 9259 (2012).

[34] V. Kumar, R. Kumar, D. K. Shukla, S. K. Arora, I. V. Shvets, K. Singh, and R. Kumar, Spin states and glassy magnetism in LaCo$_{1-x}$Ni$_x$O$_3$ ($0 \leqslant x \leqslant 0.5$), Mater. Chem. Phys. **147**, 617 (2014).

[35] H. Kozuka, K. Ohbayashi, and K. Koumoto, Electronic conduction in La-based perovskite-type oxides, Sci. Technol. Adv. Mater. **16**, 026001 (2015).

[36] M. Viswanathan and P. S. Anil Kumar, Observation of reentrant spin glass behavior in LaCo$_{0.5}$Ni$_{0.5}$O$_3$, Phys. Rev. B **80**, 012410 (2009).

[37] W. Huang, C. Tian, J. Meng, N. Xu, Y. Zhang, L. Zhao, and H. Zhong, Highly efficient and stable intermediate-temperature solid oxide fuel cells using PrCo$_{0.5}$Ni$_{0.5}$O$_{3-\delta}$ cathode, J. Phys. Chem. C **128**, 10826 (2024).

[38] V. Kumar, R. Kumar, D. K. Shukla, S. Gautam, K. H. Chae, and R. Kumar, Electronic structure and electrical transport properties of LaCo$_{1-x}$Ni$_x$O$_3$ ($0 \leqslant x \leqslant 0.5$), J. Appl. Phys. **114**, 073704 (2013).

[39] H. W. Brinks, H. Fjellvag, A. Kjekshus, and B. C. Hauback, Structure and magnetism of Pr$_{1-x}$Sr$_x$CoO$_{3-\delta}$, J. Solid State Chem. **147**, 464 (1999).

[40] M. R. Ibarra, R. Mahendiran, C. Marquina, B. Garcia-Landa, and J. Blasco, Huge anisotropic magnetostriction in La$_{1-x}$Sr$_x$CoO$_{3-\delta}$ (x $>\sim$ 0.3): Field-induced orbital instability, Phys. Rev. B **57**, R3217 (1998).

[41] https://jp-minerals.org/vesta/en/.

[42] K. Momma and F. Izumi, VESTA: A three-dimensional visualization system for electronic and structural analysis, J. Appl. Crystallogr. **41**, 653 (2008).

[43] F. Reinert, P. Steiner, S. Hüfner, H. Schmitt, J. Fink, M. Knupfer, P. Sandl, and E. Bertel, Electron and hole doping in NiO, Z. Phys. B **97**, 83 (1995).

[44] J. C. Rojas Sánchez, B. Nelson-Cheeseman, M. Granada, E. Arenholz, and L. B. Steren, Exchange-bias effect at La$_{0.75}$Sr$_{0.25}$MnO$_3$/LaNiO$_3$ interfaces, Phys. Rev. B **85**, 094427 (2012).

[45] K. Chen, C. Luo, B. B. Chen, R. M. Abrudan, G. Koster, S. K. Mishra, and F. Radu, Charge-transfer-induced interfacial ferromagnetism in $La_{0.7}Sr_{0.3}MnO_3/NdNiO_3$, Phys. Rev. Mater. **4**, 054408 (2020).

[46] Z. Hu, H. Wu, M. W. Haverkort, H. H. Hsieh, H.-J. Lin, T. Lorenz, J. Baier, A. Reichl, I. Bonn, C. Felser, A. Tanaka, C. T. Chen, and L. H. Tjeng, Different look at the spin state of Co^{3+} ions in a CoO_5 pyramidal coordination, Phys. Rev. Lett. **92**, 207402 (2004).

[47] S. G. Minasian, E. R. Batista, C. H. Booth, D. L. Clark, J. M. Keith, S. A. Kozimor, W. W. Lukens, R. L. Martin, D. K. Shuh, S. C. E. Stieber, T. Tylisczcak, and X.-D. Wen, Quantitative evidence for lanthanide-oxygen orbital mixing in CeO_2, PrO_2, and TbO_2, J. Am. Chem. Soc. **139**, 18052 (2017).

[48] Z. Hu, G. Kaindl, H. Ogasawara, A. Kotani, and I. Felner, Ln-4f/ligand-2p covalence in $BaLnO_3$ and Cs_3LnF_7 (Ln = Ce, Pr, Tb), Chem. Phys. Lett. **325**, 241 (2000).

[49] J. Padilla-Pantoja, J. Herrero-Martín, P. Gargiani, S. M. Valvidares, V. Cuartero, K. Kummer, O. Watson, N. B. Brookes, and J. L. García-Muñoz, Stability of the cationic oxidation states in $Pr_{0.50}Sr_{0.50}CoO_3$ across the magnetostructural transition by X-ray absorption spectroscopy, Inorg. Chem. **53**, 8854 (2014).

[50] B. T. Thole, G. van der Laan, J. C. Fuggle, G. A. Sawatzky, R. C. Karnatak, and J.-M. Esteva, $3d$ x-ray-absorption lines and the $3d^9 4f^{n+1}$ multiplets of the lanthanides, Phys. Rev. B **32**, 5107 (1985).

[51] F. Guillou, K. Kummer, Y. Bréard, L. Hervé, and V. Hardy, Valence and spin-state transition in cobaltates revisited by x-ray magnetic circular dichroism, Phys. Rev. B **95**, 174445 (2017).

[52] C. F. Chang, Z. Hu, H. Wu, T. Burnus, N. Hollmann, M. Benomar, T. Lorenz, A. Tanaka, H.-J. Lin, H. H. Hsieh, C. T. Chen, and L. H. Tjeng, Spin blockade, orbital occupation, and charge ordering in $La_{1.5}Sr_{0.5}CoO_4$, Phys. Rev. Lett. **102**, 116401 (2009).

[53] K. Knížek, P. Novák, and Z. Jirák, Spin state of $LaCoO_3$: Dependence on CoO_6 octahedra geometry, Phys. Rev. B **71**, 054420 (2005).

[54] J. M. Rondinelli and N. A. Spaldin, Structural effects on the spin-state transition in epitaxially strained $LaCoO_3$ films, Phys. Rev. B **79**, 054409 (2009).

[55] Y. Kobayashi, S. Murata, K. Asai, J. M. Tranquada, and G. Shirane, and K. Kohn, Magnetic and transport properties of $LaCo_{1-x}Ni_xO_3$—Comparison with $La_{1-x}Sr_xCoO_3$, J. Phys. Soc. Jpn. **68**, 1011 (1999).

[56] E. Lee, D. H. Kim, H. W. Kim, J. D. Denlinger, H. Kim, J. Kim, K. Kim, B. I. Min, B. H. Min, Y. S. Kwon, and J.-S. Kang, The 7×1 Fermi surface reconstruction in a two-dimensional f-electron charge density wave system: $PrTe_3$, Sci. Rep. **6**, 30318 (2016).

[57] M.-J. Huang, G. Deng, Y. Y. Chin, Z. Hu, J.-G. Cheng, F. C. Chou, K. Conder, J.-S. Zhou, T.-W. Pi, J. B. Goodenough, H.-J. Lin, and C. T. Chen, Determination of hole distribution in $Sr_{14-x}Ca_xCu_{24}O_{41}$ using soft x-ray absorption spectroscopy at the Cu L_3 edge, Phys. Rev. B **88**, 014520 (2013).

[58] F. Guillou, Q. Zhang, Z. Hu, C. Y. Kuo, Y. Y. Chin, H. J. Lin, C. T. Chen, A. Tanaka, L. H. Tjeng, and V. Hardy, Coupled valence and spin state transition in $(Pr_{0.7}Sm_{0.3})_{0.7}Ca_{0.3}CoO_3$, Phys. Rev. B **87**, 115114 (2013).

[59] C. Wu, Y. Sun, Z. Yang, J. Hu, T.-Y. Ding, J. Cheng, and K. H. L. Zhang, Tuning the spin state of Co^{3+} by crystal facet engineering for enhancing the oxygen evolution reaction activity, Chem. Mater. **34**, 10509 (2022).

[60] A. Chikamatsu, T. Katayama, T. Maruyama, M. Kitamura, K. Horiba, H. Kumigashira, H. Wadati, and T. Hasegawa, Investigation of the electronic states of a-site layer-ordered double perovskite $YBaCo_2O_x$ ($x = 5.3$ and 6) thin films by x-ray spectroscopy, Appl. Phys. Lett. **118**, 012401 (2021).

[61] Q. Che, M. Ghiasi, L. Braglia, M. L. J. Peerlings, S. Mauri, P. Torelli, P. de Jongh, and F. M. F. de Groot, Operando soft x-ray absorption of $LaMn_{1-x}Co_xO_3$ perovskites for CO oxidation, ACS Catal. **14**, 11243 (2024).

[62] Y. Bitla, Y.-Y. Chin, J.-C. Lin, C. N. Van, R. Liu, Y. Zhu, H.-J. Liu, Q. Zhan, H.-J. Lin, C.-T. Chen, Y.-H. Chu, and Q. He, Origin of metallic behavior in $NiCo_2O_4$ ferrimagnet, Sci. Rep. **5**, 15201 (2015).

[63] Z. Hu, H. Wu, T. C. Koethe, S. N. Barilo, S. V. Shiryaev, G. L. Bychkov, C. Schüßler-Langeheine, T. Lorenz, A. Tanaka, H. H. Hsieh, *et al.*, Spin-state order/disorder and metal–insulator transition in $GdBaCo_2O_{5.5}$: Experimental determination of the underlying electronic structure, New J. Phys. **14**, 123025 (2012).

[64] Y. Cao, X. Liu, M. Kareev, D. Choudhury, S. Middey, D. Meyers, J.-W. J.-W. Kim, P. J. Ryan, J. W. Freeland, and J. Chakhalian, Engineered Mott ground state in a $LaTiO_{3+\delta}/LaNiO_3$ heterostructure, Nat. Commun. **7**, 10418 (2016).

[65] T. Mizokawa and A. Fujimori, Electronic structure and orbital ordering in perovskite-type $3d$ transition-metal oxides studied by Hartree-Fock band-structure calculations, Phys. Rev. B **54**, 5368 (1996).

[66] M. L. Medarde, Structural, magnetic and electronic properties of $RNiO_3$ perovskites (R = rare earth), J. Phys.: Condens. Matter **9**, 1679 (1997).

[67] Z. Ali, I. Ahmad, B. Amin, M. Maqbool, G. Murtaza, I. Khan, M. J. Akhtar, and F. Ghaffor, Theoretical studies of structural and magnetic properties of cubic perovskites $PrCoO_3$ and $NdCoO_3$, Physica B **406**, 3800 (2011).

[68] M. Bernal-Salamanca, J. Javier Herrero-Martín, Z. Konstantinović, L. Balcells, A. Pomar, B. Martínez, and C. Frontera, X-ray absorption spectroscopy study of thickness effects on the structural and magnetic properties of $Pr_{2-\delta}Ni_{1-x}Mn_{1+x}O_{6-y}$ double perovskite thin films, Nanomaterials **12**, 4337 (2022).

[69] R. Kadono, M. Miyazaki, M. Hiraishi, H. Okabe, A. Koda, K. Amemiya, and H. Nakao, Direct observation of oxygen polarization in Sr_2IrO_4 by O K-edge x-ray magnetic circular dichroism, Phys. Rev. B **107**, L201122 (2023).

[70] E. Goering, A. Bayer, S. Gold, G. Schütz, M. Rabe, U. Rüdiger, and G. Güntherodt, Direct correlation of Cr $3d$ orbital polarization and O K-edge X-ray magnetic circular dichroism of epitaxial CrO_2 films, Europhys. Lett. **58**, 906 (2002).

[71] T. Koide, H. Miyauchi, J. Okamoto, T. Shidara, T. Sekine, T. Saitoh, A. Fujimori, H. Fukutani, M. Takano, and Y. Takeda, Close correlation between the magnetic moments, lattice distortions, and hybridization in $LaMnO_3$ and $La_{1-x}Sr_xMnO_{3+\delta}$: Doping-dependent magnetic circular x-ray dichroism study, Phys. Rev. Lett. **87**, 246404 (2001).

[72] T. Tsuyama, T. Matsuda, S. Chakraverty, J. Okamoto, E. Ikenaga, A. Tanaka, T. Mizokawa, H. Y. Hwang, Y. Tokura, and H. Wadati, X-ray spectroscopic study of $BaFeO_3$ thin films: An Fe^{4+} ferromagnetic insulator, Phys. Rev. B **91**, 115101 (2015).

[73] D. Fuchs, M. Merz, P. Nagel, R. Schneider, S. Schuppler, and H. v. Löhneysen, Double exchange via t_{2g} orbitals and the Jahn-Teller effect in ferromagnetic $La_{0.7}Sr_{0.3}CoO_3$ probed by epitaxial strain, Phys. Rev. Lett. **111**, 257203 (2013).

[74] S. Medling, Y. Lee, H. Zheng, J. F. Mitchell, J. W. Freeland, B. N. Harmon, and F. Bridges, Evolution of magnetic oxygen states in Sr-doped $LaCoO_3$, Phys. Rev. Lett. **109**, 157204 (2012).

[75] K. Feldmann, K. Hennig, L. Kaun, B. Lippold, M. M. Lukina, S. Matthies, W. Matz, and E. Warming, Crystal field levels of Pr^{3+} in $PrFeO_3$ and $PrGaO_3$ determined by inelastic neutron scattering, Phys. Stat. Sol. (b) **72**, 817 (1975).

[76] P. Novák, K. Knížek, M. Maryško, Z. Jirák, and J. Kuneš, Crystal field and magnetism of Pr^{3+} and Nd^{3+} ions in orthorhombic perovskites, J. Phys.: Condens. Matter **25**, 446001 (2013).

[77] Z Jirák, J. Hejtmánek, K. Knížek, M. Maryško, P. Novák, E. Šantavá, T. Naito, and H. Fujishiro, Ground-state properties of the mixed-valence cobaltites $Nd_{0.7}Sr_{0.3}CoO_3$, $Nd_{0.7}Ca_{0.3}CoO_3$ and $Pr_{0.7}Ca_{0.3}CoO_3$, J. Phys.: Condens. Matter **25**, 216006 (2013).

[78] L. V. Pourovskii, A. Alena Vishina, O. Eriksson, and K. M. I., Quantitative theory of magnetic properties of elemental praseodymium, npj Comput Mater **11**, 326 (2025).

[79] A. Panfilov, G. Grechnev, A. Lyogenkaya, V. Pashchenko, I. Zhuravleva, L. Vasylechko, V. Hreb, V. Turchenko, and D. Novoselov, Magnetic properties of $RCoO_3$ cobaltites (R = La, Pr, Nd, Sm, Eu). Effects of hydrostatic and chemical pressure, Physica B **553**, 80 (2019).

[80] I. Vobornik, L. Perfetti, M. Zacchigna, M. Grioni, G. Margaritondo, J. Mesot, M. Medarde, and P. Lacorre, Electronic-structure evolution through the metal-insulator transition in $RNiO_3$, Phys. Rev. B **60**, R8426 (1999).

[81] D. D. K., A. Singh, S. Sathapathy, K. K. Maurya, P. K. Siwach, V. K. Malik, S. S. Kushvaha, and H. K. Singh, Large magnetoresistance in $PrNiO_3$ thin film deposited by RF magnetron sputtering, J. Supercond. Novel Magn. **36**, 623 (2023).

[82] J. E. Rodrigues, A. D. Rosa, J. Gainza, R. S. Silva, E. Mijit, G. Garbarino, T. Irifune, T. Shinmei, C. Dejoie, N. M. Nemes, *et al.*, Mapping pressure- and temperature-induced structural and magnetic transitions in perovskite $PrNiO_3$ with local and long-range probes, Chem. Mater. **36**, 596 (2024).

[83] P. H. Wagner, V. Metlushko, L. Trappeniers, A. Vantomme, J. Vanacken, G. Kido, V. V. Moshchalkov, and Y. Bruynseraede, Magnetotransport in epitaxial thin films of the magnetic perovskite $Pr_{0.5}Sr_{0.5}MnO_3$, Phys. Rev. B **55**, 3699 (1997).

[84] S. C and W. F, Ferromagnetic ordering with high Curie temperature in a new Pr_2FeNiO_6 double perovskite material, J. Supercond. Novel Magn. **35**, 2867 (2022).

[85] R. Booth, R. Fillman, H. Whitaker, A. Nag, R. Tiwari, K. Ramanujachary, J. Gopalakrishnan, and S. Lofland, An investigation of structural, magnetic and dielectric properties of R_2NiMnO_6 (R = rare earth, Y), Mater. Res. Bull. **44**, 1559 (2009).

[86] G. Zhang, G. Li, F. Liao, Y. Fu, M. Xiong, and J. Lin, Crystal growth and magnetic properties of the double perovskites R_2MnNiO_6 (R = Pr, Sm and Ho) by a hydrothermal route, J. Cryst. Growth **327**, 262 (2011).

[87] T. Chakraborty, H. Nhalil, R. Yadav, A. A. Wagh, and S. Elizabeth, Magnetocaloric properties of R_2NiMnO_6 (R = Pr, Nd, Tb, Ho and Y) double perovskite family, J. Magn. Magn. Mater. **428**, 59 (2017).

[88] M. P. Singh, K. D. Truong, S. Jandl, and P. Fournier, Magnetic properties and phonon behavior of Pr_2NiMnO_6 thin films, Appl. Phys. Lett. **98**, 162506 (2011).

[89] B. T. Thole, P. Carra, F. Sette, and G. van der Laan, X-ray circular dichroism as a probe of orbital magnetization, Phys. Rev. Lett. **68**, 1943 (1992).

[90] P. Carra, B. T. Thole, M. Altarelli, and X. Wang, X-ray circular dichroism and local magnetic fields, Phys. Rev. Lett. **70**, 694 (1993).

[91] H. Wende, Recent advances in x-ray absorption spectroscopy, Rep. Prog. Phys. **67**, 2105 (2004).

[92] W. Yang, M. Rosenkranz, G. Velkos, F. Ziegs, V. Dubrovin, S. Schiemenz, L. Spree, M. F. de Souza Barbosa, C. Guillemard, *et al.*, Covalency versus magnetic axiality in Nd molecular magnets: Nd-photoluminescence, strong ligand-field, and unprecedented nephelauxetic effect in fullerenes $NdM_2N@C_{80}$ (M = Sc, Lu, Y), Chem. Sci. **15**, 2141 (2024).

[93] C. T. Chen, Y. U. Idzerda, H.-J. Lin, N. V. Smith, G. Meigs, E. Chaban, G. H. Ho, E. Pellegrin, and F. Sette, Experimental confirmation of the x-ray magnetic circular dichroism sum rules for iron and cobalt, Phys. Rev. Lett. **75**, 152 (1995).

[94] H. C. Su, M.-J. Huang, H.-J. Lin, C.-H. Lee, C.-T. Chen, C.-H. Liu, H.-F. Hsu, K.-W. Lin, and J. van Lierop, Connection between orbital moment enhancement and exchange bias in a $[Ni_{80}Fe_{20}/Mn]_3$ multilayer, Phys. Rev. B **87**, 014402 (2013).

[95] X. Yin, M. A. Majidi, X. Chi, P. Ren, L. You, N. Palina, X. Yu, C. Diao, D. Schmidt, B. Wang, *et al.*, Unraveling how electronic and spin structures control macroscopic properties of manganite ultra-thin films, NPG Asia Mater. **7**, e196 (2015).

[96] S. Tripathi, XMCD investigation at $M_{4,5}$-edges of the rare earth elements in high-performance permanent magnet, Ph.D. thesis, Universität Stuttgart, 2018.

[97] P. Shirazi, T. Lee, M. K. Panduranga, A. T. N'Diaye, A. Barra, and G. P. Carman, Rare-earth orbital moment contributions to the magnetic anisotropy in magnetostrictive $Tb_{0.3}Dy_{0.7}Fe_2$, Appl. Phys. Lett. **118**, 162401 (2021).

[98] C. Piamonteze, P. Miedema, and F. M. F. de Groot, Accuracy of the spin sum rule in XMCD for the transition-metal L edges from manganese to copper, Phys. Rev. B **80**, 184410 (2009).

[99] Y. Teramura, A. Tanaka, and T. Jo, Effect of coulomb interaction on the x-ray magnetic circular dichroism spin sum rule in 3*d* transition elements, J. Phys. Soc. Jpn. **65**, 1053 (1996).